Prediction of seismic wave dispersion and attenuation from ultrasonic velocity measurements

Fuyong Yan[1], De-hua Han[1], Qiuliang Yao[1], and Luanxiao Zhao[1]

ABSTRACT

Dispersion and attenuation are important attributes of seismic data that can provide important information about reservoir rock lithology, pore fluid type, and pore structure. Based on Cheng's pore-aspect-ratio spectrum inversion methodology, we related the closure and deformation of soft pores to the measured pressure-dependent porosity data. With this additional constraint, the inverted pore-aspect-ratio spectrum and concentrations are more realistic. The complex pore structure controls two important intrinsic dispersion and attenuation mechanisms: Biot flow and squirt flow. We modified and extended Tang's unified velocity dispersion and attenuation model and made it applicable to poroelastic media with a complex pore structure under the undrained condition. The inverted pore-aspect-ratio spectra from pressure-dependent ultrasonic velocity measurements were put into the modified Tang's model to predict velocity dispersion and attenuation in full frequency range at various differential pressure conditions.

INTRODUCTION

It is generally believed that the pressure dependency of rock seismic velocities is primarily caused by the sequential closing of cracks or soft pores (Nur, 1969; Toksöz et al., 1976; Cheng, 1978). Although these cracks (also called *soft pores*) usually are volumetrically small, they can have significant saturation effect (Toksöz et al., 1976) on seismic velocities. Yan et al. (2013) discuss the effect of complicated pore geometry on Gassmann fluid substitution. The soft pores are also believed to be important for velocity dispersion and attenuation of porous rocks. During the passing of pressure waves, the dispersion induced by the interaction of pore fluids between soft pores and stiff pores might be much stronger than that induced by the Biot flow as shown in the ultrasonic measurement data by Han (1986). Several dual-porosity (crack and stiff pore) mathematical models (Dvorkin et al., 1995; Chapman et al., 2002; Wei and Muraleetharan, 2006; Tang, 2011; Tang et al., 2012) are brought up to describe the dispersion and attenuation phenomena related to fluid interaction between soft crack pores and stiff pores. The double-porosity model (Pride and Berryman, 2003a, 2003b; Berryman, 2006) can describe dispersion and attenuation caused by heterogeneity of different scales. In this study, we only study the dispersion and attenuation induced by the squirt flow and Biot flow. It is also possible to measure the velocity dispersion and attenuation of porous rock as a function of frequency in the laboratory (Spencer, 1981; Batzle et al., 2006), but this technology is still in development and the measurement is much more expensive than the conventional ultrasonic velocity measurement.

The pore structure of real rock is much more complicated than a dual-porosity model (crack and stiff pores). One way to describe the complex pore system is using the pore-aspect-ratio spectrum. Based on Eshelby's (1957) ellipsoidal inclusion theory and the Kuster and Toksöz (1974) model, Cheng (1978) tries to use the pressure-dependent ultrasonic velocity data to invert the pore-aspect-ratio spectrum. The pore spectrum could also be derived from mercury-injection data or nuclear-magnetic-resonance-logging data. If we know the pore structure and the pore fluids, theoretically, we should be able to predict the frequency dependent behavior of seismic velocities of porous rocks. This study is to explore the feasibility of predicting velocity dispersion and attenuation at a wide frequency range using pressure-dependent ultrasonic velocity and pore volume change measurement data.

SYNOPSIS OF CHENG'S PORE-ASPECT-RATIO SPECTRUM-INVERSION METHODOLOGY

Based on Eshelby's (1957) study of the elastic stress-strain field around an ellipsoidal inclusion, Cheng (1978) derives the volume fractional change of the inclusion,

$$\frac{dc}{c} = -\frac{P_e/K^*}{E_1 - \dfrac{E_2 E_3}{E_3 + E_4}}, \tag{1}$$

where $E_1 = 3\mu I_a / \pi (3K + 4\mu)$, $E_2 = 3\mu / (2\pi(3K + 4\mu))(3I_a - 4\pi)$, $E_3 = \alpha^2[3 - (9I_a/4\pi)][3K + \mu]/([1 - \alpha^2][3K + 4\mu]) + 3\mu I_a/[4\pi(3K + 4\mu)]$, $E_4 = [(3 - 9I_a/(4\pi))(3K + \mu)/2(1 - \alpha^2)(3K + 4\mu)] - [3(1 - \pi/I_a)/2(3K + 4\mu)]$, $I_a = [2\pi\alpha/(1 - \alpha^2)^{3/2}][\cos^{-1}(\alpha) - \alpha\sqrt{(1 - \alpha)}]$, c is the volume fraction of the inclusion, P_e is the effective pressure, K^* is the effective bulk modulus, K and μ are the bulk modulus and shear modulus of the solid rock frame, respectively, and α is the aspect ratio of the inclusion. If $(dc/c) \leq -1$, then the crack is assumed to be closed. Equation 1 states that the pore volume change is a function of the pore-aspect ratio and effective pressure if the solid rock frame elastic properties are known. Concentration of a certain group of cracks at pressure p_n is related to its concentration at zero effective pressure by

$$c_{nm} = c_{0m}\left(1 + \frac{dc}{c}(\alpha_{0m}, p_n)\right). \tag{2}$$

In this section and the next, the subscript n means that the parameter is pressure dependent and m means that the parameter is a function of the pore-aspect ratio; subscript 0 refers to the status of zero effective pressure. If we assume the crack (pore) is in the shape of a spheroid and the primary change of the crack is the variation of the shortest axis in response to the applied stress field, we have

$$\frac{d\alpha}{\alpha} = \frac{dc}{c}. \tag{3}$$

Thus, we can relate the pore-aspect-ratio change to its status at zero effective pressure by

$$\alpha_{nm} = \alpha_{0m}\left(1 + \frac{d\alpha}{\alpha}(\alpha_{0m}, p_n)\right) = \alpha_{0m}\left(1 + \frac{dc}{c}(\alpha_{0m}, p_n)\right). \tag{4}$$

From equations 2 and 4, the volume concentration of a certain type of crack and its aspect ratio at any pressure can be related by

$$c_{nm} = \frac{c_{0m}}{\alpha_{0m}}\alpha_{nm}. \tag{5}$$

In summary, equations 1–5 describe how concentration and shape of pores with a certain initial volume and aspect-ratio change with applied stress field. By assumption of the spheroidal shape and primary deformation in the direction of the shortest axis, the change of the aspect ratio is equal to the fractional pore concentration change. Both changes are related to its initial status (zero effective pressure), so that we only need to know the pore-aspect-ratio spectrum at one stress status (e.g., the zero effective pressure condition), then the pore-aspect-ratio spectrum at any pressure condition can be calculated using equations 1–5. These treatments and simplification are critical and make it possible to invert the pore-aspect-ratio spectrum from the pressure-dependent ultrasonic velocity measurements.

Considering higher concentration and possible effects of crack interaction, the effective elastic moduli of solid matrix with multiple ellipsoidal inclusions are estimated by the extended Kuster-Toksöz theory by Cheng (1978) that can be written in simple matrix form as

$$\sum_{m=1}^{M} c_{nm}P_{nm} = b_{Kn}, \quad \sum_{m=1}^{M} c_{nm}Q_{nm} = b_{Gn}, \tag{6}$$

using the notation

$$b_{Kn} = \frac{K_n^* - K}{K' - K} \cdot \frac{3K_n^* - 4\mu}{3K + 4\mu},$$
$$b_{Gn} = \frac{\mu_n^* - \mu}{\mu' - \mu} \cdot \frac{6\mu_n^*(K + 2\mu) + \mu(9K + 8\mu)}{25\mu(3K + 4\mu)}, \tag{7}$$

where the elastic moduli without superscript are for the solid rock frame, the moduli with the prime symbol (') are for the inclusion, and * indicates the effective modulus, and

$$P_{nm} = \frac{1}{3}T_{iijj}(\alpha_{nm}), \quad Q_{nm} = T_{ijij}(\alpha_{nm}) - \frac{1}{3}T_{iijj}(\alpha_{nm}), \tag{8}$$

where T_{iijj} and T_{ijij} are the scalar functions of the pore-aspect-ratio and elastic moduli of the background medium. Their expressions can be found in the appendices of papers by Kuster and Toksöz (1974), Toksöz et al. (1976), Cheng (1978), and Cheng and Toksöz (1979).

Substituting equation 5 into 6, we get

$$\sum_{m=1}^{M} \alpha_{nm}P_{nm}\frac{c_{0m}}{\alpha_{0m}} = b_{Kn}, \quad \sum_{m=1}^{M} \alpha_{nm}Q_{nm}\frac{c_{0m}}{\alpha_{0m}} = b_{Gn}. \tag{9}$$

This is a linear equation system in the form of $A\mathbf{x} = \mathbf{b}$. Here, α_{0m} is given and α_{nm} can be calculated based on the given α_{0m} using equation 4, and x_m (equal to c_{0m}/α_{0m}) is the actual root to be solved. The pore-aspect-ratio spectrum at any pressure can be computed from the solution using equations 4 and 5.

PRESSURE-DEPENDENT POROSITY CONSTRAINT

Cheng (1978) uses different approaches to solve the linear equation system (equation 9). Constant porosity constraints of different forms are used in his solving approaches. This is a paradox because the algorithms in the last section basically describe how the pore volume change (by deformation and opening/closing of cracks of different pore-aspect ratios) affects the elastic properties when the effective pressure is changed. As we discussed earlier, this small pore volume change can have a significant effect on the elastic properties of rocks and should not be neglected; thus, including pressure-dependent porosity data is important for reliable inversion of the pore-aspect-ratio spectra. Although the total pore volume change is usually small (approximately 0.1–0.5 ml for a typical reservoir rock sample of 1–1/2 in. diameter), it can be measured simultaneously during conventional pressure-dependent ultrasonic velocity measurements (Han, 1986). One simple way is to keep the pore pressure constant and measure amount of pore fluid (usually brine) absorbed from the digital pump at each confining pressure

decrease. Depending on the model, the digital pump can read pore fluid volume change as small as 2.5 nanoliters.

From equation 5, it is straightforward that the total porosity at any pressure can be formulated by

$$\phi_{tn} = \sum_{m=1}^{M} c_{nm} = \sum_{m=1}^{M} \frac{c_{0m}}{\alpha_{0m}} \alpha_{nm}. \quad (10)$$

We can combine equation 10 with equation 9 to make the inverted pore-aspect-ratio spectra at different pressures comply with measured porosity change data and make the inverted results more realistic. The final linear system becomes

$$\begin{pmatrix} \alpha_{11} & \alpha_{12} & \cdots & \alpha_{1M} \\ \alpha_{21} & \alpha_{22} & \cdots & \alpha_{2M} \\ \vdots & \vdots & \vdots & \vdots \\ \alpha_{N1} & \alpha_{N2} & \cdots & \alpha_{NM} \\ \alpha_{11}P_{11} & \alpha_{12}P_{12} & \cdots & \alpha_{1M}P_{1M} \\ \alpha_{21}P_{21} & \alpha_{22}P_{22} & \cdots & \alpha_{2M}P_{2M} \\ \vdots & \vdots & \vdots & \vdots \\ \alpha_{N1}P_{N1} & \alpha_{N2}Q_{N2} & \cdots & \alpha_{NM}Q_{NM} \\ \alpha_{11}Q_{11} & \alpha_{12}Q_{12} & \cdots & \alpha_{1M}Q_{1M} \\ \alpha_{21}Q_{21} & \alpha_{22}Q_{22} & \cdots & \alpha_{2M}Q_{2M} \\ \vdots & \vdots & \vdots & \vdots \\ \alpha_{N1}Q_{N1} & \alpha_{N2}Q_{N2} & \cdots & \alpha_{NM}Q_{NM} \end{pmatrix} \begin{pmatrix} \frac{c_{01}}{\alpha_{01}} \\ \frac{c_{02}}{\alpha_{02}} \\ \vdots \\ \frac{c_{0M}}{\alpha_{0M}} \end{pmatrix} = \begin{pmatrix} \phi_{t1} \\ \phi_{t2} \\ \vdots \\ \phi_{tN} \\ b_{K1} \\ b_{K2} \\ \vdots \\ b_{KN} \\ b_{G1} \\ b_{G2} \\ \vdots \\ b_{GN} \end{pmatrix}, \quad (11)$$

where N is the number of pressure measurement points and M is the number of elements of pore-aspect-ratio spectrum.

MODIFICATION AND EXTENSION OF TANG'S MODEL

Within the framework of the Biot theory, Tang (2011) brings up a unified model to describe wave propagation in porous media affected by the Biot flow and squirt flow. Similar to the Biot-squirt (BISQ) model (Dvorkin and Nur, 1993; Dvorkin et al., 1995), the high-frequency limit of Tang's model is equivalent to that of the Biot theory, and the low limit of the Tang's model is below the low limit of the Biot-Gassman theory and close to the drained low limit predicted by the BISQ model. So Tang's model is for the drained condition and is not applicable to the general subsurface scenarios for seismic exploration (Yao, 2013).

For rocks under subsurface conditions, if we assume the wavelength is much larger than the grain size, compared with the Biot flow, the communication of pore fluids between cracks and stiff pores is more eligible to be treated as local flow in closed boundary. As long as the pore fluids are not completely relaxed, the effective bulk modulus should always be higher than that predicted by the Biot-Gassmann theory. At the high-frequency limit, the pore fluids in the cracks are locked and the cracks are effectively stiff, so the velocity is higher than the high limit predicted by the Biot-Gassmann theory. At the low-frequency limit, the pore fluids in cracks are completely relaxed (reaches pressure balance with pore fluid in stiff pores), the cracks are effectively soft, then the velocity should be

equal to that predicted by the Gassmann equation (low limit of the Biot theory). Under this principle, following Tang's procedure, we have rederived and modified Tang's model as

$$K^* = K_d + \frac{n^2}{(n-\phi)/K_m + (\phi/K_f) - \Delta S(\omega)}, \quad (12)$$

where K^* is the effective bulk modulus without considering the effect of the Biot flow, K_d is the dry bulk modulus, and n is the Biot coefficient. The detailed derivation can be found in Yao's (2013) dissertation. Here, $\Delta S(\omega)$ is the term related to squirt flow and instantaneous storage capacity of the cracks, and it is represented by

$$\Delta S(\omega) = S_{\max} - S(\omega), \quad (13)$$

where

$$S_{\max} = \frac{8\pi\varepsilon K_d(\nu_m - 1)(K^* - K_m)}{3K_m\mu_m(K^* - K_d)}, \quad (14)$$

$$S(\omega) = \frac{(8/3)\pi\varepsilon((1-\nu_m)/\mu_m)f(\varsigma)\left(\frac{1/K_d - 1/K_m}{1/K_d - 1/K^*} - f(\varsigma)\right)}{1 + \frac{4(1-\nu_m)K_f}{3\alpha\mu_m}(1 - f(\varsigma))}, \quad (15)$$

with

$$f(\varsigma) = \frac{2J_1(\varsigma)}{\varsigma J_0(\varsigma)}, \quad (16)$$

$$\varsigma = \sqrt{\frac{3i\omega\eta}{\alpha^2 K_f}}, \quad (17)$$

where ω is the angular frequency, η is the pore fluid viscosity, α is the pore-aspect ratio, ν_m is the Poisson's ratio of the background medium, and ε is the crack density, which is defined by

$$\varepsilon = \frac{\phi_c}{2\pi\alpha}, \quad (18)$$

where ϕ_c is the concentration of cracks with pore-aspect-ratio α and $S_{\max}$ is the term related to maximum fluid volume that can be transferred from cracks to stiff pores if the cracks are completely relaxed ($\omega \to 0$).

Similar to the treatment of the differential effective medium (DEM) model (Cleary et al., 1980; Norris, 1985), for multiple inclusions of cracks with different aspect ratios, the effect of cracks can be added differentially to the system and the effective modulus (K^*) is updated iteratively. Because the squirt flow is a nonlinear process, the differential scheme is more rational because it considers the pore pressure increase in stiff pores when the pore fluid in soft pores is squeezed into the stiff pores. The original Tang's (2011) model assumes the pore pressure in stiff pores does not increase when the pore fluid in soft pores is squeezed into the stiff pores.

Therefore, the original Tang's (2011) model might break at moderate low-crack density because of overestimation of the squirt flow. The modified Tang's model using differential scheme does not break at high crack density. The final computed effective modulus (K^*) is substituted into the Biot theory formulated by Tang and Cheng (2004) to calculate wave velocities under the influence of Biot flow and squirt flow. The velocity dispersion and attenuation can be calculated by (Tang, 2011)

$$v = \frac{\omega}{\text{Re}[k]}, \qquad (19)$$

$$Q^{-1} = \frac{2\,\text{Im}[k]}{\text{Re}[k]}, \qquad (20)$$

where Q is the quality factor, k is the wavenumber, and $\text{Re}[k]$ and $\text{Im}[k]$ are the real part and imaginary part of k, respectively.

APPLICATION EXAMPLE

The rock physics measurement data of sample Berea 5-600 from Han (1986) are used to test the feasibility of the methodology we introduced in this study. This sandstone sample has porosity approximately 19.5%, clay content of 6%, and permeability of 495 md (Yale, 1984). Other input parameters for pore-aspect-ratio spectra inversion are the mineral elastic moduli: For quartz, $K = 37$ GPa, $\mu = 40$ GPa and for clay, $K = 25$ GPa, $\mu = 7$ GPa. The bulk modulus of water is 2.25 GPa.

The general procedure is that first, we invert the pore-aspect-ratio spectrum at zero effective pressure using equation 11, then use
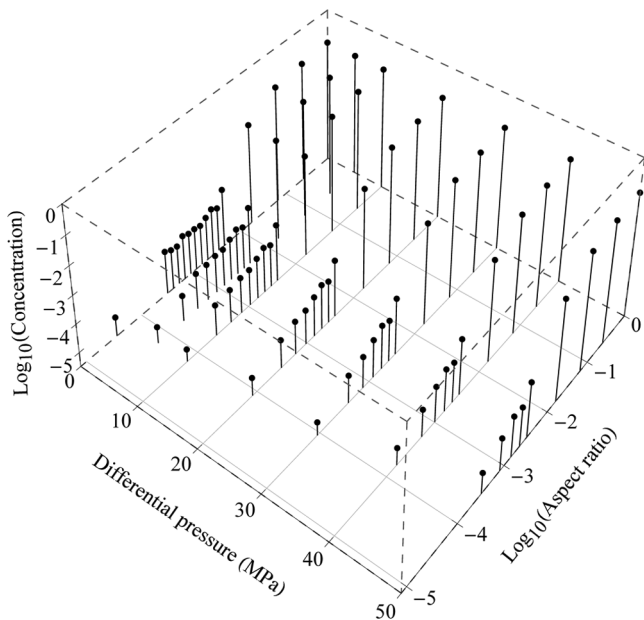

Figure 1. Pore-aspect-ratios spectra at different differential pressures. The concentrations of stiffer pores (with a higher aspect ratio) change little with increasing differential pressure; the concentrations of softer pores (crack, with a lower aspect ratio) decrease with increasing differential pressure, and even close sequentially with increasing differential pressure.

equations 4 and 5 to compute the pore-aspect-ratio spectrum at different differential pressures, and last, the pore-aspect-ratio spectra are put into the modified Tang's model to predict velocity dispersion and attenuation. The extra input parameters for prediction of velocity dispersion and attenuation are pore fluid viscosity of 1 cP and tortuosity of 2.4.

The pore-aspect-ratio elements α_{0m} are given, and what we really inverted by equation 11 are the corresponding concentrations c_{0m}. The α_{0m} determines how the complex pore system is represented. Cheng (1978) states that selection of α_{0m} is primarily determined by the pressure range and the pressure increments of the data. Under this general guideline, he made detailed sensitivity analysis and stated that the inversion results are not very sensitive to choice of α_{0m}. In this study, we first use equation 1 to estimate two closing pore-aspect-ratios (α_L and α_H) at 5 and 500 MPa. The velocity data will not be sensitive to cracks with aspect ratio less than α_L, so we use only one element to represent this type of cracks. The velocity data will be most sensitive to cracks with aspect ratio between α_L and α_H and less sensitive to cracks with aspect ratio between α_H and 1.0.

As shown in Figure 1, the pore-aspect-ratio elements at zero differential pressure are logarithmically evenly spaced between the interval of α_L to α_H and interval of α_H to 1.0, and they are denser in the former interval because the velocity data are most sensitive to them. In total, 16 elements of pore-aspect-ratio are used. We suggest that equation 11 be treated as an overdetermined inversion problem. For future applications, we suggest that the pressure increment be reduced by half. The inverted pore-aspect-ratios and concentrations at different differential pressures ($P_d = 0$, 5, 10, 20, 30, 40, and 50 MPa, respectively) are shown in Figure 1. As shown in the figure, the concentrations of stiffer pores (with higher aspect ratio) change little with increasing differential pressure; the concentrations of softer pores (cracks, with lower aspect ratio) decrease with increasing differential pressure, and even close sequentially with increasing differential pressure. The detailed values for the modeled pore-aspect-ratio spectra at different differential pressures are shown in Tables 1 and 2.

Figure 2 shows a comparison between the measured and modeled pore volume change. The pressure-dependent porosities are estimated from the digital pump reading when the pore pressure is kept constant and the confining pressure decreases. With the decreasing of confining pressure, the pore volume increases and more fluids will be absorbed into the pore system from the reservoir tank of the digital pump. The volume of the reservoir tank of the digital pump is monitored and displayed in real time, with resolution that can be as high as 2.5 nanoliters depending on the digital pump model. The total pore volume change for the core sample in this study is approximately 0.2 ml in the pressure range of measurement. As long as the pore pressure is kept constant, the estimated pore volume change will not be affected by pore fluid compressibility. Thus, it is possible to monitor the total pore volume change while the routine ultrasonic measurements are conducted. The fitting of the measured porosities and modeled porosities (sum of concentrations of different pore-aspect-ratios at a certain differential pressure) indicates the theoretical rationality of the pore-aspect-ratio spectrum inversion methodology.

Figure 3 shows the comparison between measured and modeled ultrasonic velocities (100% water saturation). The upper data points and curve are for the P-wave velocity, and the lower data points and

curve are for the S-wave velocity. Basically, the modeled velocities are computed using Kuster-Toksöz's (1974) theory and the inverted pore-aspect-ratio spectra.

The pore volume change due to closure and deformation of crack pores generally agrees with the measured porosity change, and the pressure-dependent velocity data can be modeled with good match; thus, we have reasonable confidence in the inverted pore-

aspect-ratio spectra. The inverted pore-aspect-ratio spectra are then put into the modified Tang's model to predict velocity dispersion and attenuation.

Figure 4 shows the prediction of fast P-wave velocity dispersion at different differential pressures. The solid curves are predicted by the modified Tang's model (considering Biot flow and squirt flow), and the dashed lines are velocity dispersion predicted by the Biot

Table 1. Pore-aspect ratios at different differential pressures.

P_d (MPa)	0	5	10	20	30	40	50
	0.99000	0.98927	0.98869	0.98776	0.98680	0.98582	0.98497
	0.25615	0.25580	0.25553	0.25509	0.25463	0.25417	0.25377
	0.06627	0.06597	0.06573	0.06536	0.06496	0.06456	0.06421
	0.01715	0.01685	0.01661	0.01623	0.01584	0.01544	0.01509
	0.00444	0.00413	0.00388	0.00348	0.00308	0.00266	closed
	0.00341	0.00309	0.00284	0.00244	0.00203	0.00160	closed
	0.00261	0.00230	0.00204	0.00164	0.00122	closed	closed
	0.00201	0.00168	0.00142	0.00101	0.00059	closed	closed
α_{nm}	0.00154	0.00121	0.00095	0.00053	closed	closed	closed
	0.00118	0.00085	0.00058	0.00016	closed	closed	closed
	0.00091	0.00057	0.00030	closed	closed	closed	closed
	0.00070	0.00035	0.00008	closed	closed	closed	closed
	0.00053	0.00019	closed	closed	closed	closed	closed
	0.00041	0.00006	closed	closed	closed	closed	closed
	0.00031	closed	closed	closed	closed	closed	closed
	0.00003	closed	closed	closed	closed	closed	closed

Table 2. Variation of volume concentrations of pores with different aspect ratios.

P_d (MPa)	0	5	10	20	30	40	50
	0.07199	0.07194	0.07190	0.07183	0.07176	0.07169	0.07163
	0.06138	0.06130	0.06123	0.06112	0.06102	0.06090	0.06081
	0.04639	0.04618	0.04601	0.04575	0.04547	0.04519	0.04495
	0.01200	0.01179	0.01163	0.01136	0.01109	0.01081	0.01057
	0.00036	0.00034	0.00032	0.00028	0.00025	0.00022	0
	1.12E-04	0.000102	9.37E-05	8.06E-05	6.69E-05	5.29E-05	0
	1.52E-04	1.33E-04	1.19E-04	9.51E-05	7.07E-05	0	0
	1.10E-04	9.19E-05	7.78E-05	5.54E-05	3.21E-05	0	0
c_{nm}	8.27E-05	6.51E-05	5.10E-05	2.87E-05	0	0	0
	9.30E-05	6.68E-05	4.59E-05	1.27E-05	0	0	0
	9.35E-05	5.87E-05	3.10E-05	0	0	0	0
	1.15E-04	5.85E-05	1.36E-05	0	0	0	0
	7.18E-05	2.55E-05	0	0	0	0	0
	7.90E-05	1.19E-05	0	0	0	0	0
	1.03E-04	0	0	0	0	0	0
	1.49E-05	0	0	0	0	0	0
ϕ_{tn}	0.19315	0.19216	0.19152	0.19062	0.18976	0.18886	0.18795

theory. Data points at 10^6 Hz are measured ultrasonic P-wave velocities at corresponding differential pressures and full water saturation. It can be seen that the predictions match well with the measured ultrasonic P-wave velocities. At low differential pressure, the dispersion caused by squirt flow dominates that caused by the Biot flow. With increasing of differential pressure, soft pores are being gradually closed and the dispersion caused by the squirt flow decreases. The characteristics of fast P-wave velocity dispersion at low-differential pressure comply with the laboratory observation (Batzle et al., 2006).

The corresponding fast P-wave attenuation is shown in Figure 5. The attenuation induced by the squirt flow is dominant at low differential pressure and can occur at a wide frequency range, whereas the Biot flow is dominant at high differential pressure and occurs at a narrow and high frequency range. At low differential pressure, the magnitude of attenuation induced by the squirt flow is much stronger than that induced by the Biot flow.
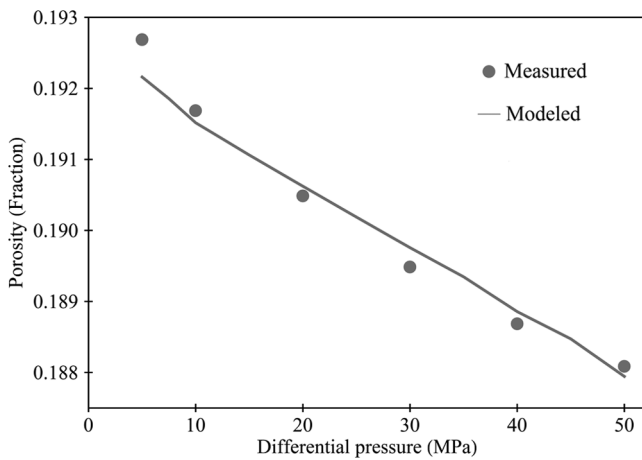
Figure 2. Comparison between measured and modeled pore volume change for sample Berea 5-600 from Han's (1986) data. All of the following plots are based on measurement and modeling of this sample. The modeled pore volume at a certain differential pressure is the summation of concentrations of the open cracks and stiff pores.
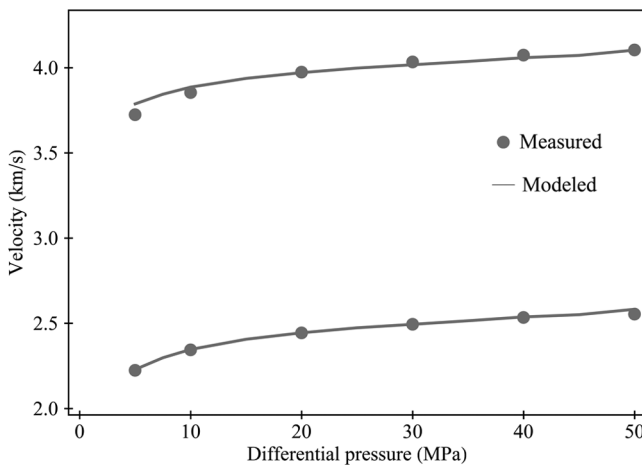
Figure 3. Comparison between measured and modeled ultrasonic velocities (100% water saturation). The upper data points and curve are for the P-wave velocity, and the lower data points and curve are for the S-wave velocity.

Figures 6 and 7 show the prediction of S-wave velocity dispersion and attenuation at different differential pressures. The solid curves are predicted by the modified Tang's model, dashed lines are velocity dispersion predicted by the Biot theory. Data points at 10^6 Hz are measured ultrasonic S-wave velocities at different differential pressures and full water saturation. As shown by the figure, S-wave attenuation induced by the squirt flow is negligible compared with that induced by the Biot flow. From Figure 7, the attenuation induced by the squirt flow occurs at wider frequency range but the magnitude is much less than that caused by the Biot
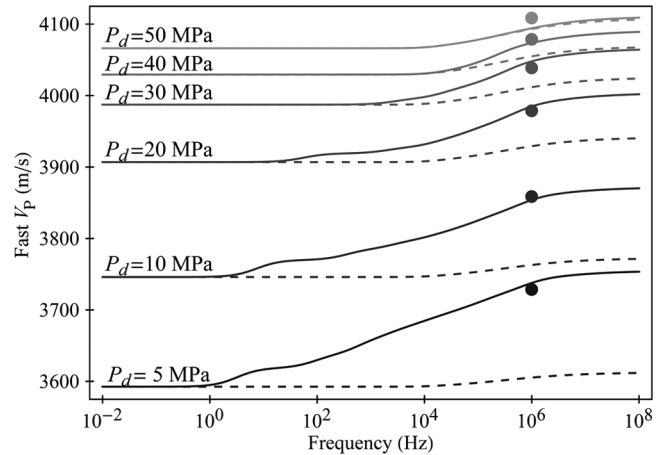

Figure 4. Prediction of fast P-wave velocity dispersion at different differential pressures. Solid curves are predicted by the modified Tang's model; dashed lines are velocity dispersion predicted by the Biot theory. Data points at 10^6 Hz are measured ultrasonic P-wave velocities at different differential pressures and full water saturation. The lighter color represents higher differential pressure, and the solid curves are predicted by the modified Tang's model and the dashed curves are predicted by the Biot theory. The color scheme and curve style have the same denotations for the following figures.
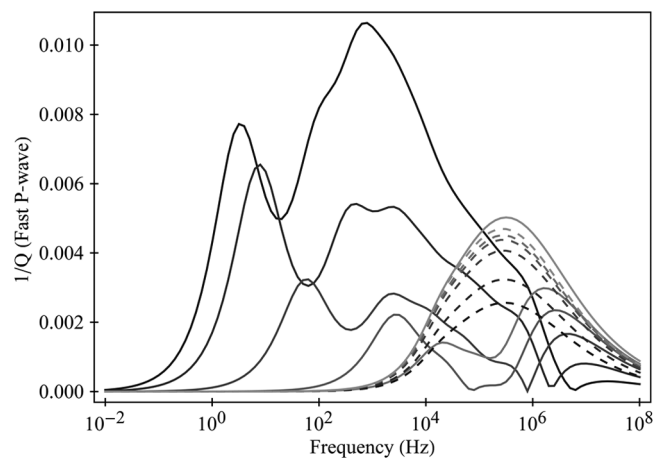

Figure 5. Fast P-wave attenuation curves corresponding to Figure 4. The attenuation induced by the squirt flow is dominant at low differential pressure and can occur at a wide frequency range. The Biot flow is dominant at high differential pressure and occurs at a narrow and high frequency range. At low differential pressure, the magnitude of attenuation induced by the squirt flow is much stronger than that induced by the Biot flow.

flow. Comparing Figures 4 and 5 with Figures 6 and 7, it is found that the squirt flow has much more influence on dispersion and attenuation of the fast P-wave than those of the S-wave.

For theoretical completeness, we also show the prediction of slow P-wave velocity dispersion and attenuation at different differential pressures (Figures 8 and 9). From the small difference between solid curves and dashed curves, the influence of the squirt flow on slow P-wave velocity dispersion is negligible. The slow P-wave velocity dispersion is dominantly controlled by the Biot flow even when most of the cracks are open. From Figure 9, the difference between the solid curves (Biot flow and squirt flow) and the dashed curves (Biot flow only) is almost indiscernible; thus, the influence of the squirt flow on slow P-wave velocity attenuation is negligible. The attenuation of slow P-wave is dominantly controlled by the Biot flow.

In summary, the modeling results show that the squirt flow has insignificant influence on dispersion and attenuation for an S-wave and a slow P-wave. For a fast P-wave, the effect of squirt flow on

dispersion and attenuation can be dominant, especially at lower pressure conditions when most of the cracks are open. The modified and extended Tang's (2011) model give rational theoretical interpretation of seismic wave dispersion and attenuation induced by the squirt flow and Biot flow for reservoir rocks with complex pore structure.

DISCUSSIONS

Tang et al. (2012) bring up a different squirt flow model based on different physical model and more simplifications. The earlier model (Tang, 2011) is based on a penny-shaped crack surrounded by stiff pore and the latter model is based on an annular crack surrounding the stiff pore. As Tang et al. (2012) state, the two models
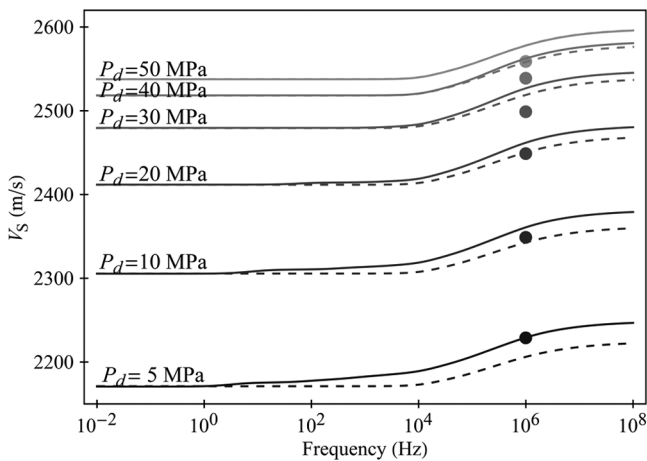

Figure 6. Prediction of S-wave velocity dispersion at different differential pressures. Data points at 10^6 Hz are measured ultrasonic S-wave velocities at different differential pressures and full water saturation.

Figure 8. Prediction of slow P-wave velocity dispersion at different differential pressures. From the small difference between solid curves and dashed curves, the influence of differential pressure and squirt flow on the slow P-wave velocity dispersion is negligible. The slow P-wave velocity dispersion is dominantly controlled by the Biot flow.
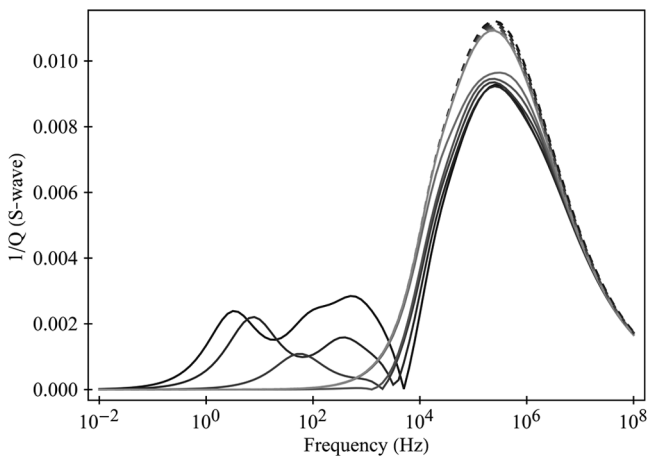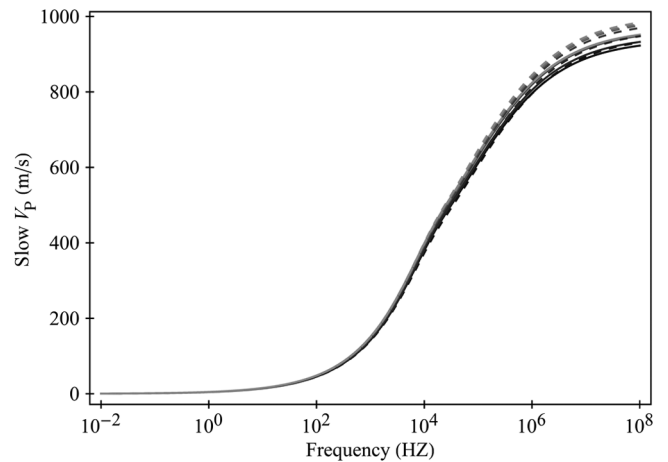

Figure 7. S-wave attenuation curves corresponding to Figure 6. The attenuation induced by the squirt flow occurs at a wider frequency range, but the magnitude is much less than that caused by the Biot flow.
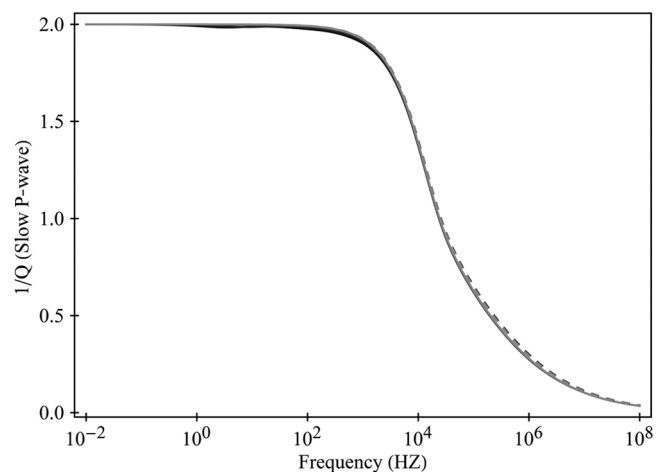

Figure 9. Slow P-wave attenuation curves corresponding to Figure 8. From the almost-indiscernible difference between the solid curves and dashed curves, the influence of differential pressure and squirt flow on the slow P-wave velocity attenuation is negligible. The attenuation of the slow P-wave is dominantly controlled by the Biot flow.

produce similar results. Because the previous model is more theoretically rigorous, so our study is based on Tang's (2011) model.

The pore-aspect-ratio spectrum inversion has theoretical limitations as discussed in detail in Cheng's (1978) thesis. One of the primary limitations is to use dynamic elastic moduli to approximate static elastic moduli. Therefore, this methodology might not work for unconsolidated rocks. It is also necessary to point out that the pressure-dependent velocities might also include significant contribution of cracks induced by stress unloading and sample handling. However, significant change of stress condition due to injection from the wells might also induce a large number of cracks in the reservoir.

Compared with low-frequency measurement, which is expensive and technically immature at present, prediction of seismic wave dispersion and attenuation from ultrasonic velocity measurements is an almost costless by-product of conventional ultrasonic velocity measurements. This study will help us to better understand the mechanism of attenuation caused by wave induced fluid flow. It can be used for better correlation between core data, log data, and seismic data. For a certain reservoir, seismic wave attenuation is pressure dependent, so time lapse seismic attenuation study might be applied for reservoir monitoring.

CONCLUSIONS

Closure and deformation of soft pores of different pore-aspect ratios are realistically related to the measured pore volume changes while conventional ultrasonic velocity testing is conducted. The complicated pore structure can be effectively modeled by the pore-aspect-ratio spectrum. The pressure-dependent ultrasonic velocity data contain important information about the fluid induced dispersion and attenuation properties of reservoir rocks. The adapted and extended Tang's model can give sound theoretical interpretation of seismic wave dispersion and attenuation induced by the squirt flow and the Biot flow. This study should help us to have better understanding of the characteristics of fluid induced seismic wave attenuation and dispersion.

ACKNOWLEDGMENTS

REFERENCES

Batzle, M. L., D.-h. Han, and R. Hofmann, 2006, Fluid mobility and frequency-dependent seismic velocity — Direct measurements: Geophysics, **71**, no. 1, N1–N9, doi: 10.1190/1.2159053.

Berryman, J. G., 2006, Effective medium theories for multicomponent poroelastic composites: Journal of Engineering Mechanics, **132**, 519–531, doi: 10.1061/(ASCE)0733-9399(2006)132:5(519).

Chapman, M., S. V. Zatsepin, and S. Crampin, 2002, Derivation of a microstructural poroelastic model: Geophysical Journal International, **151**, 427–451, doi: 10.1046/j.1365-246X.2002.01769.x.

Cheng, C. H., 1978, Seismic velocities in porous rocks — Direct and inverse problems: Ph.D. thesis, MIT.

Cheng, C. H., and M. N. Toksöz, 1979, Inversion of seismic velocities for the pore aspect ratio spectrum of a rock: Journal of Geophysical Research, **84**, 7533–7543, doi: 10.1029/JB084iB13p07533.

Cleary, M. P., I. W. Chen, and S. M. Lee, 1980, Self-consistent techniques for heterogeneous media: Journal of the Engineering Mechanics Division, American Society of Civil Engineers, **106**, 861–887.

Dvorkin, J., G. Mavko, and A. Nur, 1995, Squirt flow in fully saturated rocks: Geophysics, **60**, 97–107, doi: 10.1190/1.1443767.

Dvorkin, J., and A. Nur, 1993, Dynamic poroelasticity: A unified model with the squirt and the Biot mechanisms: Geophysics, **58**, 524–533, doi: 10.1190/1.1443435.

Eshelby, J. D., 1957, The determination of the elastic field of an ellipsoidal inclusion, the related problems: Proceedings of the Royal Society of London, Series A, **241**, 376–396, doi: 10.1098/rspa.1957.0133.

Han, D.-H., 1986, Effects of porosity and clay content on acoustic properties of sandstones and consolidated sediments: Ph.D. thesis, Stanford University.

Kuster, G. T., and M. N. Toksöz, 1974, Velocity and attenuation of seismic waves in two phase media: Geophysics, **39**, 587–606, doi: 10.1190/1.1440450.

Norris, A. N., 1985, A differential scheme for the effective moduli of composites: Mechanics of Materials, **4**, 1–16, doi: 10.1016/0167-6636(85)90002-X.

Nur, A., 1969, Effects of stress and fluid inclusions on wave propagation in rocks: Ph.D. thesis, MIT.

Pride, S. R., and J. G. Berryman, 2003a, Linear dynamics of double-porosity dual-permeability materials: I. Governing equations and acoustic attenuation: Physical Review E, **68**, 036603, doi: 10.1103/PhysRevE.68.036603.

Pride, S. R., and J. G. Berryman, 2003b, Linear dynamics of double-porosity dual-permeability materials: II. Fluid transport equations: Physical Review E, **68**, 036604, doi: 10.1103/PhysRevE.68.036604.

Spencer, J. W., 1981, Stress relaxations at low frequencies in fluid saturated rocks: Attenuation and modulus dispersion: Journal of Geophysical Research, **86**, 1803–1812, doi: 10.1029/JB086iB03p01803.

Tang, X. M., and A. Cheng, 2004, Quantitative borehole acoustic methods: Elsevier Science Publishing Co.

Tang, X. M., 2011, A unified theory for elastic wave propagation through porous media containing cracks — An extension of Biot's poroelastic wave theory: Science China Earth Sciences, **54**, 1441–1452, doi: 10.1007/s11430-011-4245-7.

Tang, X. M., X.-L. Chen, and X.-K. Xu, 2012, A cracked porous medium elastic wave theory and its application in interpreting acoustic data from tight formations: Geophysics, **77**, no. 6, D245–D252, doi: 10.1190/geo2012-0091.1.

Toksöz, M. N., C. H. Cheng, and A. Timur, 1976, Velocities of seismic waves in porous rocks: Geophysics, **41**, 621–645, doi: 10.1190/1.1440639.

Wei, C., and K. K. Muraleetharan, 2006, Acoustical characterization of fluid-saturation porous media with local heterogeneities: Theory and application: International Journal of Solids and Structures, **43**, 982–1008, doi: 10.1016/j.ijsolstr.2005.06.008.

Yale, L. B. (compiler), 1984, Rock catalog: Stanford rock physics: vol. 1, Stanford University.

Yan, F., D.-h. Han, and Q. Yao, 2013, Effective porosity for Gassmann fluid substitution: 83rd Annual International Meeting, SEG, Expanded Abstracts, 2861–2865.

Yao, Q., 2013, Velocity dispersion and wave attenuation in reservoir rocks: Ph.D. thesis, University of Houston.